Journal of
Synchrotron
Radiation

ISSN 1600-5775

Received 22 January 2014
Accepted 11 April 2014

Hard X-ray nanotomography beamline 7C XNI at PLS-II

Jun Lim,[a]* Hyounggyu Kim[b] and So Yeong Park[c]

[a]Beamline Division, Pohang Light Source, Hyoja, Pohang, Kyung-buk 790784, Republic of Korea, [b]School of Information and Mechatronics, GIST, 123 Cheomdan, Buk-gu, Gwangju 500712, Republic of Korea, and [c]Department of Physics, POSTECH, Hyoja, Pohang, Kyung-buk 790784, Republic of Korea.
*E-mail: limjun@postech.ac.kr

The synchrotron-based hard X-ray nanotomography beamline, named 7C X-ray Nano Imaging (XNI), was recently established at Pohang Light Source II. This beamline was constructed primarily for full-field imaging of the inner structures of biological and material samples. The beamline normally provides 46 nm resolution for still images and 100 nm resolution for tomographic images, with a 40 μm field of view. Additionally, for large-scale application, it is capable of a 110 μm field of view with an intermediate resolution.

Keywords: X-ray nanoscopy; X-ray nanotomography; X-ray Zernike phase contrast; zone plate.

1. Introduction

Lens-based hard X-ray full-field transmission microscopy is a valuable tool for inspection of thick samples at a spatial resolution of several tens of nanometers (Yin *et al.*, 2006; Chen *et al.*, 2011*a*; Wang *et al.*, 2012). Notably, this microscopy modality, unlike electron microscopy and thanks to the high-transmission characteristic of hard X-rays, allows for *in vivo* and *in situ* experimentation with thick biosamples. However, its weak absorption negatively affects image contrast. To solve this problem the Zernike phase-contrast method, which utilizes the phase delay between zeroth-order and higher-order spatial frequencies (Zernike, 1955), has been adapted to X-ray microscopy. For this purpose, a nano-patterned thin metal ring is usually employed. An in-depth study on the phase ring's effect on image quality showed that its shape accuracy and alignment significantly influence the phase contrast (Chen *et al.*, 2011*b*). In addition, artifacts such as halo effects and shade-off arise due to the erroneous modulation of the diffracted component by the phase ring. In conventional lens-based X-ray microscopy set-ups, focusing optics such as those involving a glass capillary or a zone plate are used to illuminate a sample with high-flux X-rays. According to these optics, the illuminated beam shape is an annular ring in order to meet the requirement that the numerical aperture (NA) matches the condenser and objective optics. In terms of the field of view (FOV), the condenser optics form a strongly demagnified image of the source, which is used to illuminate the sample (critical illumination). Typically, the FOV is about 20 μm in diameter. Thus, for large-sample applications, small images have to be tiled. Such 'mosaic' images, however, show artifacts such as boundaries and residual beam structure. To date, the reported best two-dimensional (2D) resolution is less than 20 nm (Chen *et al.*, 2011*a*) and the best three-dimensional (3D) resolution is 50 nm (Wang *et al.*, 2012) with a capillary condenser optics in the hard X-ray region. Thus, the strengths of conventional lens-based X-ray microscopy are its isotropic and high resolution, and its weaknesses are its difficult alignment, small FOV and erroneous artifacts. For easier alignment and to enhance the phase-contrast effect with minimization of artifacts, the 7C XNI beamline utilizes an off-axis-illumination scheme and a point-like phase plate for microscopy (Kagoshima *et al.*, 2002; Yokosuka *et al.*, 2002); to enlarge the FOV, meanwhile, it uses a parabolic beryllium compound refractive lens (CRL). Even though the resolution is anisotropic, it has as good as 50 nm resolution in 2D and 70 nm in 3D, regardless of the NA-matching condition. Moreover, applications for large-scale (up to 110 μm diameter) samples with intermediate-resolution (~100 nm) imaging is possible. In this paper we present a detailed description of the beamline along with 2D imaging and 3D tomographic imaging performance evaluations.

2. Beamline overview

Fig. 1 shows the optical layout of the 7C XNI beamline along with a photograph of the main components (Lim *et al.*, 2013). High-flux X-rays are provided by means of a 1.4 m-long hybrid-type in-vacuum undulator with a period of 20 mm (SFA, Korea). For the 3.0 GeV and 400 mA stored-beam-current PLS-II operating parameters, the undulator provides up to 2.95 kW of X-ray power (Yu *et al.*, 2014). X-rays are monochromated ($\Delta E/E \simeq 10^{-4}$) using a liquid-nitrogen-cooled silicon (111) double-crystal monochromator (Vactron, Korea) located 18 m from the X-ray source. In front of the monochromator, a diamond window (Diamond Materials GmbH, Germany) of 1 cm diameter and 200 μm thickness reduces the thermal load on the silicon crystal. In order to focus, or rather collimate, the divergent X-rays, ten beryllium parabolic CRLs (RXOPTICS, Germany) of diameter 1 mm and effective aperture ~0.6 mm (reduced by absorption), positioned 25.7 m downstream from the source, are employed. At that position, the FWHM beam size is 2.1 mm × 0.7 mm. The focal length of each CRL is 3.25 m at 6.7 keV, and the focused beam size is 70 μm × 10 μm. The beam shape is due mainly to the undulator source, which is of a vertically small but horizontally large size (560 μm × 80 μm). The estimated photon flux at the focus position is $\sim 10^{11}$ photons s^{-1}, as calculated by measuring the air

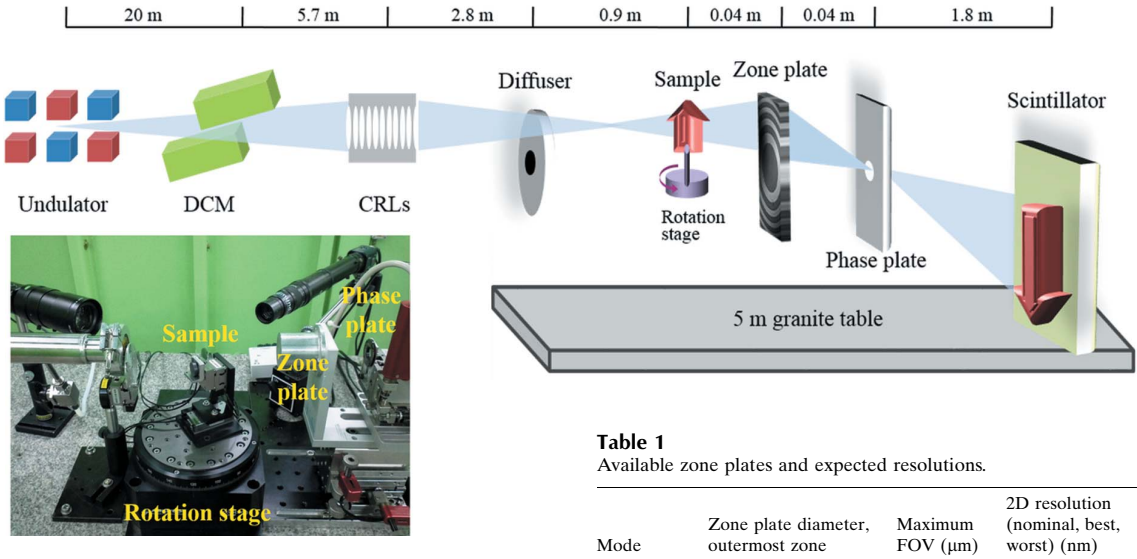

Figure 1
Optical layout of the 7C XNI beamline and photograph of the main part.

currents in an ionization chamber. In order to reduce the spatial coherency and homogenize the illumination, a diffuser (rotating paper) is inserted in front of the sample. Next, to define the illumination, a pinhole of diameter 40 µm is installed. The sample is mounted on a three-axis piezo-driven scanning stage (Newport; model AG-LS25) on top of an air-bearing rotation stage (Areotech; model ABRS-150MP). To expand the FOV to a 40 µm diameter, the position of the sample is moved slightly out of the focal plane of (3.5 m from) the CRLs. The rotation-stage specifications are as follows: <450 nm radial error motion; <175 nm axial error motion; <10 µrad tilt error motion. The objective zone plate, of 50 nm outermost zone width, 140 µm diameter and 1.0 µm thickness, is made of tungsten (Zoneplates, UK). The theoretically expected efficiency is ∼30%. At 6.7 keV, the first-order focal length is 40 mm. For Zernike phase contrast, a holed aluminium-film phase plate of 3.78 µm ± <0.04 µm thickness (Luxel, USA) is positioned near the back focal plane of the zone plate. The thickness is selected so as to phase shift the diffracted beam by $\pi/2$ and, thereby, make the sample image darker in the bright field. The hole, of 10 µm diameter, is drilled by focused ion beams. Note that, even with a hole size much larger than the focused beam, the phase plate significantly reduces the halo effect, because the area of phase change in the back focal plane is much smaller than when using a phase ring. The positioning system of the optical components includes ULTRAlign and Gothic Arch XYZ stages (Newport) and picomotor actuators (New Focus). The detector comprises a thin (18 µm) Tb:LSO scintillator crystal (FEE, Germany) of 10 mm diameter and an X20 homemade optical microscope. The microscope is composed of an X20 objective lens (Zeiss) and a CCD (Apogee Imaging Systems; model U16MF). The CCD has 4096 × 4096 pixels of 9 µm size. All of the optics, including the diffuser, pinhole, sample, zone plate, phase plate and detector, are installed on a 5 m-long 30 cm-thick granite plate to minimize external vibration. The beam path on the table, of the order of 10^{-3} torr, except around the sample, passes through a low-vacuum pipe. For the purpose of positioning a sample in air, Kapton film of 25 µm thickness is used to separate air from the vacuum. In the scintillator crystal, besides the positive first-order image beam, there is a zeroth-order bright beam and negative first-order fan-out beam. Since the magnification is high enough to separate each of the beams, we can image only the positive first-order image beam, using a beam stop to block the zeroth-order beam. Biological samples, such as an insect or plant stems, are of too large a size capture in a single image, and, moreover, cutting such a sample to sufficiently small dimensions presents difficulties. Therefore, in order to obtain images of large samples we utilize a large zone plate of 266 µm diameter and 66 nm outermost zone width (Zoneplates, UK). In this case, the sample is positioned 3 m from the CRLs, and the FOV is ∼110 µm in diameter. Table 1 provides a summary of the two available XNI beamline modes.

Table 1
Available zone plates and expected resolutions.

Mode	Zone plate diameter, outermost zone	Maximum FOV (µm)	2D resolution (nominal, best, worst) (nm)	3D resolution (nominal) (nm)
Normal	140 µm, 50 nm	40	46, 36, 57	100
Large-field	266 µm, 66 nm	110	114, 97, 124	160

3. Hard X-ray microscopic imaging

First, we tested the performance of the normal mode. Fig. 2(*a*) shows an image of 500 nm silica (SiO_2) spheres. This image was obtained by subtracting a slightly shifted image from the original image in order to remove background noise. As pointed out previously, the off-axis illumination scheme, known as oblique lighting, produces a 'pseudo 3D appearance' caused by the absence of one sideband of the object's diffraction light. Even though this pseudo 3D appearance lowers the contrast at the rim of the illumination, off-axis illumination with the Zernike phase method effects an outstanding contrast. In a line plot of the spheres in the central region (Fig. 2*a*, inset), the contrast enhancement, ∼95%, is clear, even though the absorption coefficient is only 2%. It should be noted that the halo effect and the shade-off effect are rarely shown. Resolution test pattern (X50-50-2, Xradia) imaging provided 46 nm spatial resolution and a 30 µm FOV (Fig. 2*b*) for an exposure time of 5 s and 922 magnification (effective pixel size: 10 nm). The spatial resolution was evaluated by power spectrum analysis (Wang *et al.*, 2012; Vogt *et al.*, 2000). Power spectrum analysis was performed on the entire test pattern and integrated azimuthally over 2π, as shown in Fig. 3(*a*). The cut-off frequency is about 12 μm^{-1}, which leads to a nominal spatial resolution (half pitch) of 46 nm (black line). More precisely, in order to quantify the anisotropic resolution of the off-axis illumination scheme, the power spectra along the two principal axes are compared. As expected, the spatial resolution along the optic axis goes down to 36 nm (red line) but along the perpendicular it is only 57 nm (blue line). Obviously, this is a main drawback of the scheme. However, the resolution

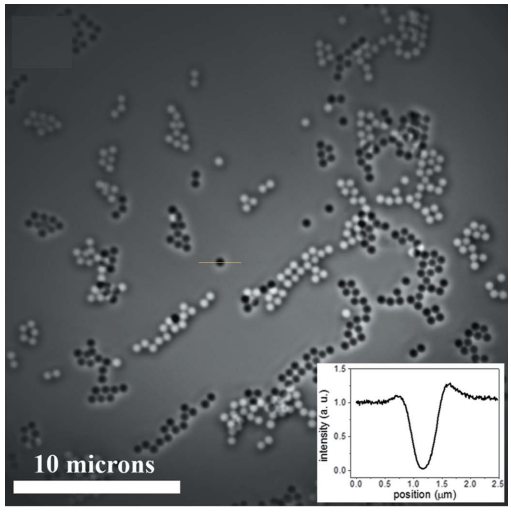

(*a*)

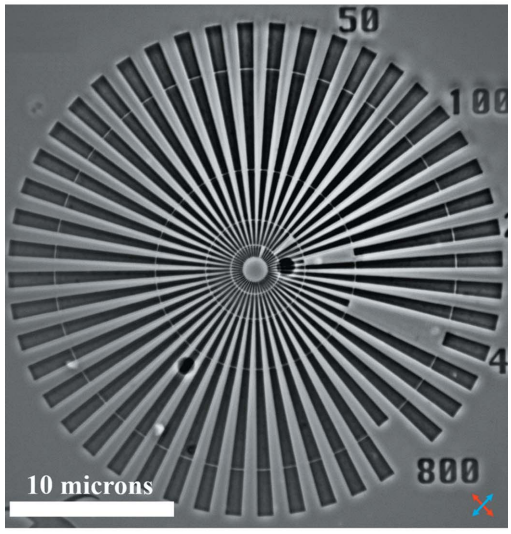

(*b*)

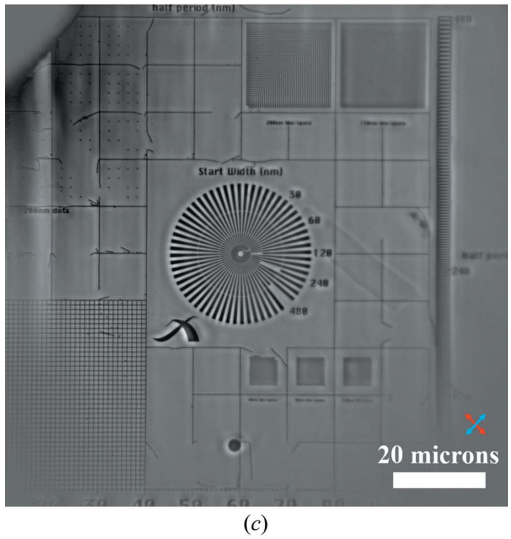

(*c*)

Figure 2
Microscopic imaging performance. (*a*) Silica spheres of 500 nm diameter in the normal mode (the inset shows a line profile of silica). (*b*) Siemens Au star test pattern with innermost features of 50 nm pitch in the normal mode. (*c*) Whole image of a resolution test pattern (Xradia, X30-30-2) in large-field mode. Red and blue arrows show the two principal axes.

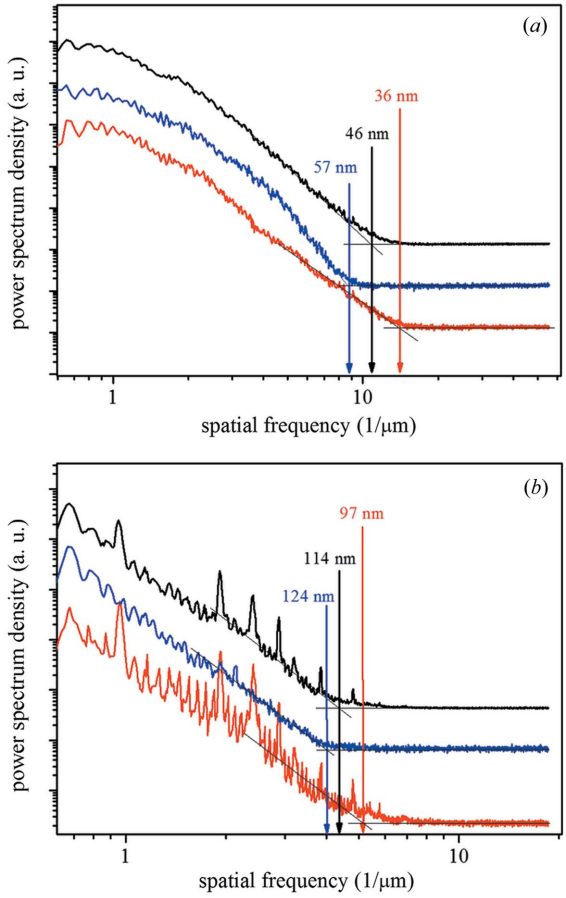

Figure 3
Power spectra of the two available modes: (*a*) normal mode and (*b*) large-field mode, taken by azimuthal integration of the frequency space image over 2π (black line). The red (best resolution) and blue lines (worst resolution) show the power spectra of the two principal axes, taken by azimuthal integration over ± 0.05 rad.

difference between the axes would be decreased if a high-resolution zone plate was used.

On the other hand, the large-field mode provides a $\sim$110 μm FOV. In order to evaluate the spatial resolution, imaging of the other resolution test pattern (X50-30-2, Xradia) was performed (Fig. 2*c*). In this case the power spectrum analysis shows that the nominal, best and worst resolutions are 114 nm (black line), 97 nm (red line) and 124 nm (blue line), respectively (Fig. 3*b*). The exposure time was (again) 5 s and the magnification was 335 (effective pixel size: 27 nm). Even though this mode has an intermediate and anisotropic spatial resolution, it is useful for investigation of large samples such as insects, stems, hair and membranes with micrometer-size pores, all of which have large-scale inner structures.

4. Hard X-ray 3D nanotomography

To date, the best commercial rotation stage incurs a wobble error (tilt motion) of $\sim$500 nrad, an eccentricity error (radial motion) of $\sim$200 nm, and an axial error of $\sim$100 nm. Thus, in order to achieve 3D nanotomography with a spatial resolution of a few tens of nanometers, the rotational motion errors of each 2D projection image from 0° to 180° should be known. Auto-alignment based on software tracking of fiducial markers (gold nanoparticles) is being used extensively to achieve automated tomography in soft X-ray microscopy and electron microscopy (Parkinson *et al.*, 2008; Le Gros *et al.*,

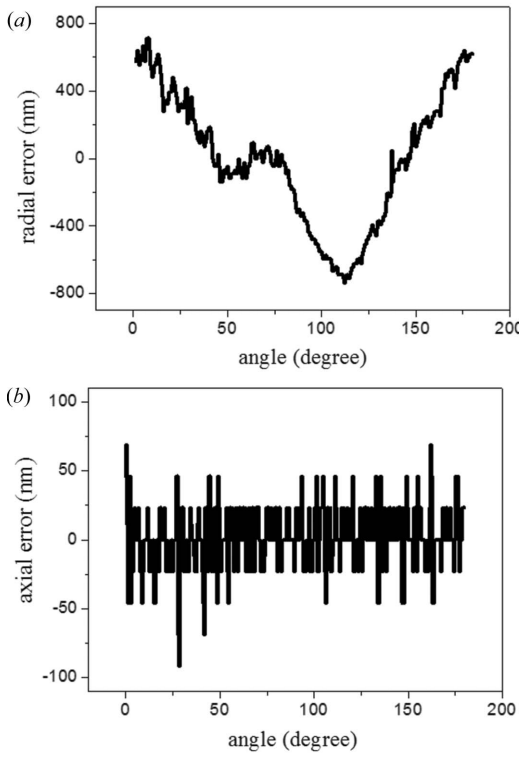

Figure 4
Experimental results of rotational errors of the air-bearing rotation stage.

2005). Very recently, markerless nanotomography systems were proposed and tested in measurements of the motion of a reference cylinder using several capacitive sensors and interferometers (Wang *et al.*, 2012; Kim *et al.*, 2013). For alignment of every 2D projection image, we adopted a method of fiducial marker (1 µm-diameter silica sphere) tracking that uses a homemade manual alignment software. Only one silica sphere, which was near the rotation axis and the center of the FOV, was used. We noted the center position of the silica sphere for each single 2D image, determined the minimum error position, and then shifted all of the images to that position. In this way, we measured the rotation error $[\Delta x(\theta), \Delta y(\theta)]$ by normal-mode imaging the silica sphere from 0° to 180° (Fig. 4). The maximum radial motion error $\Delta x(\theta)$ was ∼1500 nm, and the axial motion error $\Delta y(\theta)$ was less than 100 nm. The radial motion error $\Delta x(\theta)$ was larger than the specification (450 nm) of the rotation stage, because the tension in the cables of the three-axis piezo-driven scanning stage on top of the rotation stage incurred an error.

We demonstrated the 3D nanotomography capability using three examples. A total of 361 images were collected over an angular range of 180°. The exposure time for each image was 5 s. Normal-mode nanotomography was applied to an NMC (Ni/Mn/Co) cathode material powder. The powder and a fiducial silica sphere were attached to a thin glass capillary by electrostatic force. Fig. 5(*a*) shows the sample's 3D-rendered image. In a reconstructed slice image, many nano-pores are visible (Fig. 5*b*). Quantified evaluation of the spatial resolution was studied by the knife-edge response (10–90% criteria) of a line in the slice image (Fig. 5*b*). We obtained a 3D spatial resolution of 100 nm. This is two times lower than the 2D resolution, due primarily to a pointing error in the manual alignment process. Obviously, taking account of the anisotropic resolution in the estimation of the 3D resolution of a volume is needed. However, it is very complicated and requires further study. In the large-field mode, the samples were a human eyebrow and an atomic force microscopy (AFM) cantilever. Fig. 6 shows a human eyebrow of ∼80 µm diameter. Figs. 6(*a*) and 6(*b*) show axial and sagittal cuts through the sample, clearly revealing the internal structures (*i.e.* the medulla and the cuticles). The fiducial marker was on top of the sample (not shown here). The other sample is a silicon AFM cantilever with 1 µm silica spheres. The silica spheres are attached to the surface of the cantilever by electrostatic force. Figs. 7(*a*) and 7(*b*) show top and side views, respectively, of a stacked image of all of the reconstructed slices of the sample. For the purposes of a fiducial marker, one of the silica spheres on the tip of the cantilever was used. We determined the 3D spatial resolution for a reconstructed slice using the knife-edge method, obtaining a value of 160 nm (Fig. 8).

5. Conclusions

The hard X-ray Nano-Imaging beamline can image various sample sizes with high resolution and high contrast. Furthermore, it is a simple and easy-to-handle instrument, which makes possible *in situ* investigation of samples in various environments. In the near future,

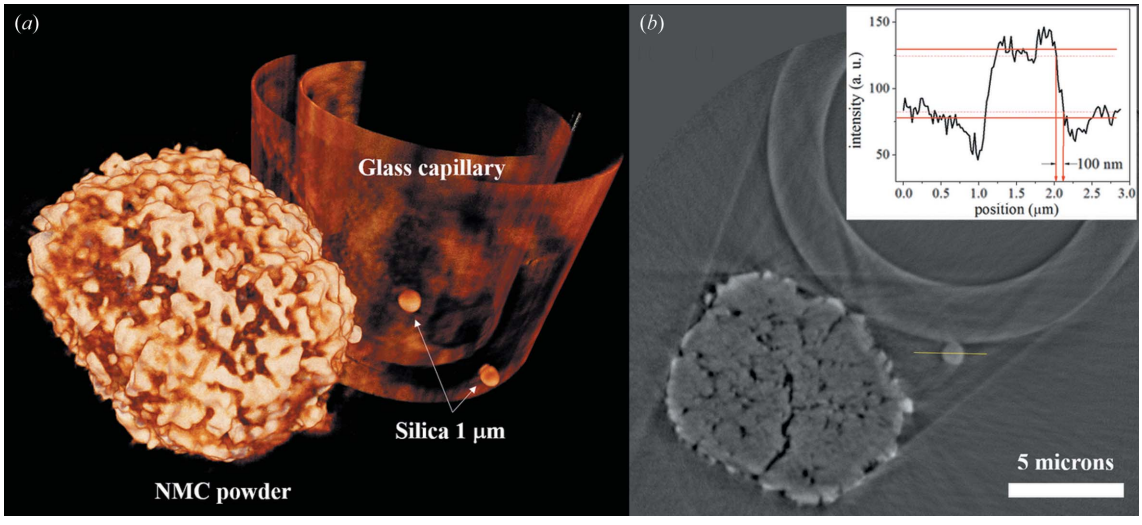

Figure 5
(*a*) 3D-rendered image of a NMC (Ni/Mn/Co) cathode material powder with reference silica spheres and glass capillary. (*b*) Section of the tomogram in the axial plane. The inset shows a line profile of a reference silica sphere; the knife-edge intensity gives 100 nm spatial resolution.

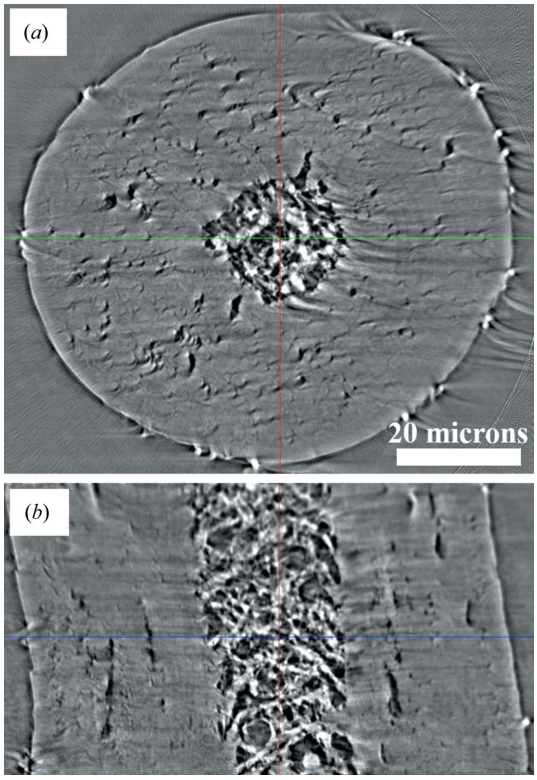

Figure 6
Part of a reconstructed slice of human eyebrow. (*a*) Axial cut, (*b*) sagittal cut.

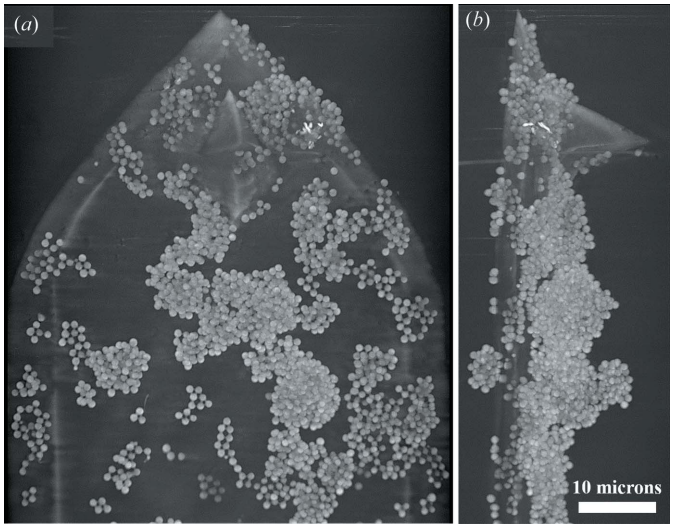

Figure 7
AFM cantilever with 1 µm silica spheres. (*a*) Top view and (*b*) side view of stacked images of all reconstructed slices.

we are planning to employ a 20 nm zone plate for tomography at a resolution approaching 20 nm.

This work was supported by the MSIP (Ministry of Science, ICT and Future Planning) of Korea.

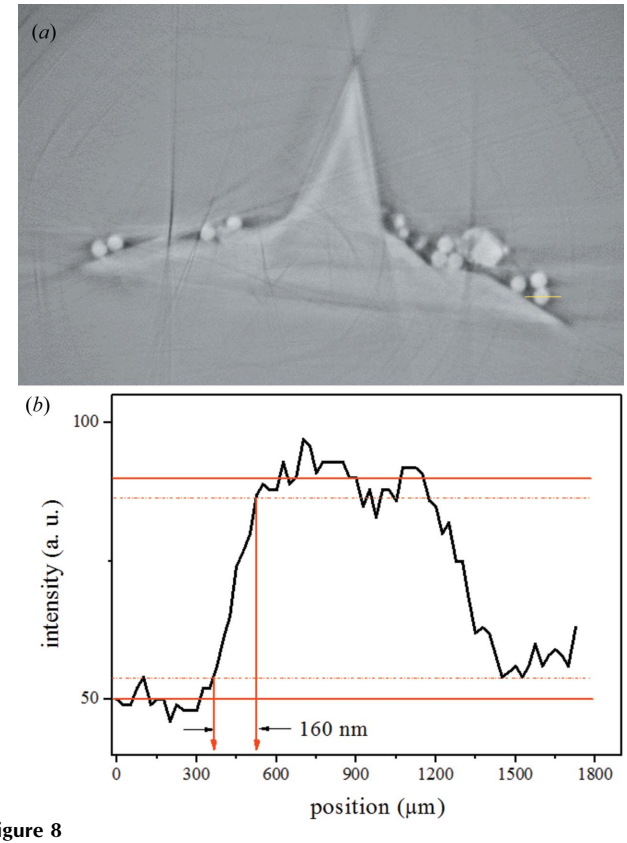

Figure 8
(*a*) Section of the tomogram perpendicular to the rotation axis. (*b*) Line profile indicated by a the yellow line in (*a*) showing 160 nm edge response using the 10–90% criteria.

References

Chen, T. Y., Chen, Y. T., Wang, C. L., Kempson, I. M., Lee, W. K., Chu, Y. S., Hwu, Y. & Margaritondo, G. (2011*a*). *Opt. Express*, **19**, 19919–19924.
Chen, Y. T., Chen, T. Y., Yi, J., Chu, Y. S., Lee, W. K., Wang, C. L., Kempson, I. M., Hwu, Y., Gajdosik, V. & Margaritondo, G. (2011*b*). *Opt. Lett.* **36**, 1269–1271.
Kagoshima, Y., Yokoyama, Y., Ibuki, T., Niimi, T., Tsusaka, Y., Takai, K. & Matsui, J. (2002). *J. Synchrotron Rad.* **9**, 132–135.
Kim, J., Lauer, K., Yan, H., Chu, Y. S. & Nazaretski, E. (2013). *Rev. Sci. Instrum.* **84**, 035006.
Le Gros, M. A., McDermott, G. & Larabell, C. A. (2005). *Curr. Opin. Struct. Biol.* **15**, 593–600.
Lim, J., Park, S. Y., Huang, J. Y., Han, S. M. & Kim, H. T. (2013). *Rev. Sci. Instrum.* **84**, 013707.
Parkinson, D. Y., McDermott, G., Etkin, L. D., Le Gros, M. A. & Larabell, C. A. (2008). *J. Struct. Biol.* **162**, 380–386.
Vogt, S., Schneider, G., Steuernagel, A., Lucchesi, J., Schulze, E., Rudolph, D. & Schmahl, G. (2000). *J. Struct. Biol.* **132**, 123–132.
Wang, J., Chen, Y. K., Yuan, Q., Tkachuk, A., Erdonmez, C., Hornberger, B. & Feser, M. (2012). *App. Phys. Lett.* **100**, 143107.
Yin, G. C., Song, Y. F., Chen, F., Tang, M. T., Liang, K. S., Duewer, F. W., Feser, M., Yun, W. & Shieh, H. P. D. (2006). *Appl. Phys. Lett.* **89**, 221122.
Yokosuka, H., Watanabe, N., Ohigashi, T., Yoshida, Y., Maeda, S., Aoki, S., Suzuki, Y., Takeuchi, A. & Takano, H. (2002). *J. Synchrotron Rad.* **9**, 179–181.
Yu, C.-J., Lee, H. C., Kim, C., Cha, W., Carnis, J., Kim, Y., Noh, D. Y. & Kim, H. (2014). *J. Synchrotron Rad.* **21**, 264–267.
Zernike, F. (1955). *Science*, **121**, 345–349.